Title
Enhanced turbulent transport and drift reduction in divertors at the detachment onset

Journal
Nuclear Fusion, 66(4)

ISSN
0029-5515

Authors
Rizkallah, Rabel
Boedo, Jose A
Tsui, Cedric K
et al.

Publication Date
2026-04-01

DOI
10.1088/1741-4326/ae4fe0

IAEA nuclear fusion

PAPER • OPEN ACCESS

Enhanced turbulent transport and drift reduction in divertors at the detachment onset

To cite this article: Rabel Rizkallah *et al* 2026 *Nucl. Fusion* **66** 046028

OPEN ACCESS
IOP Publishing | International Atomic Energy Agency

Nuclear Fusion

Nucl. Fusion **66** (2026) 046028 (17pp)

https://doi.org/10.1088/1741-4326/ae4fe0

Enhanced turbulent transport and drift reduction in divertors at the detachment onset

Rabel Rizkallah*, Jose A. Boedo, Cedric K. Tsui[a], Renato Perillo and the TCV Team[b]

Center for Energy Research, University of California San Diego (UCSD), La Jolla, San Diego, CA 92093, United States of America

E-mail: rrizkallah@ucsd.edu

Received 14 November 2025, revised 15 February 2026
Accepted for publication 10 March 2026
Published 19 March 2026

Abstract

At the onset of detachment, measurements show that radial turbulent particle transport $\left(\tilde{\Gamma}_r\right)$ increases by a factor of $2-4$ above the dissipative region in the near scrape-off layer (SOL) of both single-null (SN) and snowflake (SF) divertors. This leads to a fourfold increase in the density decay length, with broadened density profiles and flattened electron temperature (T_e) profiles along the divertor leg. These profiles are convected uniformly through the divertor by parallel flows, with parallel heat transport shifting from conduction- to convection-dominated. Within the dissipative divertor, the flattening and collapse of the plasma potential (V_p) profiles weaken electric field gradients, reducing the $E \times B$ drifts. Turbulent spreading upstream of the dissipative region thus emerges as the dominant mechanism for radial transport at the detachment onset. Radial and poloidal drifts are shown to move respectively $\sim$10%–20% and $\sim$15%–30% of the target-normal particle and heat flux delivered to the outer strike point in attached conditions, but their contribution drops to a few percent at the detachment onset.

Keywords: plasma turbulence, turbulent transport, divertor physics, divertor detachment, $E \times B$ flows, parallel transport

(Some figures may appear in colour only in the online journal)

[a] Currently affiliated with Sandia National Laboratories California, P O Box 969, Livermore, CA 94551, United states of America.
[b] See Duval *et al* 2024 (https://doi.org/10.1088/1741-4326/ad8361) for the TCV Team.
* Author to whom any correspondence should be addressed.

1. Introduction

Plasma exhaust handling remains a critical challenge for magnetically confined fusion devices, particularly next-generation reactors such as ITER [1, 2] and DEMO [3]. Divertor detachment [4, 5], a highly radiative state that cools the plasma before it reaches the material surface, is essential for mitigating plasma fluxes and protecting divertor components. In ITER, heat fluxes to the first wall will be controlled by operating a single-null (SN) divertor in a partially detached regime [6]. Unfortunately, experimental data on divertor physics, notably transport and turbulence, remains sparse, especially in detached regimes.

Simulations of detached divertors using SOLPS-[7] and SOLPS-ITER-[8] indicate that reproducing experimental profiles requires a large increase in the particle and heat diffusion coefficients in the divertor region, showing that radial transport is both significantly enhanced and anomalous. Turbulence driven by instabilities is a natural candidate for this enhanced transport. While direct observations remain limited, evidence has been reported in ASDEX Upgrade-[9] and DIII-D-[10], with measurements of divertor-localized fluctuations in Alcator C-Mod [11] and NSTX-U [12] providing direct support for increased divertor transport. Divertor-localized filaments were also shown to play an important role in broadening electron density profiles under attached conditions [13], but become less prevalent and even absent at sufficiently high collisionalities near detachment [14]. Turbulence driven instabilities are expected to arise in regions characterized by steep gradients, strong radiation fronts, and cold, dense plasma. Potential mechanisms include the current-convective instability, driven by temperature asymmetries between the inner and outer divertors [15, 16], and ionization-recombination instabilities [17]. However, these have not yet been thoroughly investigated and the available data is very limited, with no direct experimental measurements proving that turbulence drives the enhanced radial transport in the detached divertor. Cross-field transport within the divertor volume must therefore be incorporated heuristically in plasma models [18]. Existing numerical codes often rely on ad hoc adjustments to transport parameters, particularly under detached conditions, with cross-field diffusivities typically requiring orders of magnitude increases to align with experimental data [8, 19].

Another key mechanism governing divertor plasma behavior is the $E \times B$ drifts, which have been extensively investigated through both numerical simulations [20–22] and experimental studies [23–27]. To distinguish between mean drift motion and fluctuation-driven transport, the time-averaged $E \times B$ drift flows will be referred to as DC $E \times B$ (direct-current) flows in this manuscript. These DC drifts have been shown to drive convective flows through the divertor, moving about 50% of the particles and 30% of the heat between the inner and outer divertor [24], and creating a large circulation across the scrape-off layer (SOL) and X-point (XPT). In attached divertors, the DC $E \times B$ drift contribution to ion poloidal motion was shown to be comparable to, or even greater than the parallel flow contribution [27, 28]. This contribution, however, was observed to decrease in strongly detached conditions [28]. Recently, DC $E \times B$ drifts have been implicated in a bifurcated transition from attached to strongly detached outer divertor conditions [29], hinting at the critical effect they have on detachment dynamics. Experimental data are however still lacking in detached divertors, making it challenging to fully quantify the DC $E \times B$ drifts impact.

Further optimization of heat exhaust strategies beyond detachment is being sought to ensure long-term divertor performance. The snowflake (SF) divertor has been proposed as an alternative to conventional SN configurations, offering a larger divertor volume, increased collisionality, and an extended connection length $L_{\|}$ [30–32]. The SF can therefore influence the turbulence regimes, as changes in $L_{\|}$ affect the normalized collisionality Λ which appears in filamentary turbulent transport models [33, 34]. Studies show that the SF divertor is able to redistribute heat fluxes between its strike points, enhance cross-field diffusivity in the intra-null region, and broaden the heat flux widths compared to an equivalent SN divertor [27, 35, 36]. Additionally, the SF configuration has been associated with increased cross-field transport [37] and enhanced turbulent transport [36, 38]. However, recent direct measurements of radial turbulent fluxes revealed a 50% reduction in the radial turbulent particle flux in the SF divertor region compared to the SN [39], suggesting a more complex interplay between turbulence and magnetic geometry.

Given the importance of turbulence and DC $E \times B$ flows in setting divertor conditions, this work aims to provide a direct comparison of plasma fluctuation magnitudes and radial turbulent transport in SN and SF divertors under both attached and near-detached conditions. By leveraging fast reciprocating probe measurements, we assess the role of turbulence in enhancing radial transport, compare turbulence-driven fluxes to the DC $E \times B$ flows, and explore whether increased connection length in SF configurations modifies fluctuation characteristics and transport. In addition, we present a dedicated analysis of parallel heat transport, including poloidal and radial projections of the parallel heat flux, and quantify how the parallel channel contributes to overall heat redistribution relative to the cross-field channels. The results contribute to the broader effort of understanding how advanced divertor designs influence plasma exhaust dynamics.

2. Experimental setup

2.1. Plasma scenarios

Plasma discharges took place in the Tokamak á Configuration Variable (TCV) [40] with a toroidal magnetic field of $B_\phi = -1.44$ T in the forward direction ($B \times \nabla B$ pointed downward towards the divertor). All discharges were performed with a deuterium (D_2) plasma in Ohmic, unseeded conditions, with the plasma current I_p oriented in the forward direction (turning clockwise seen from the top). The vertical plasma position was systematically varied across multiple discharges, with

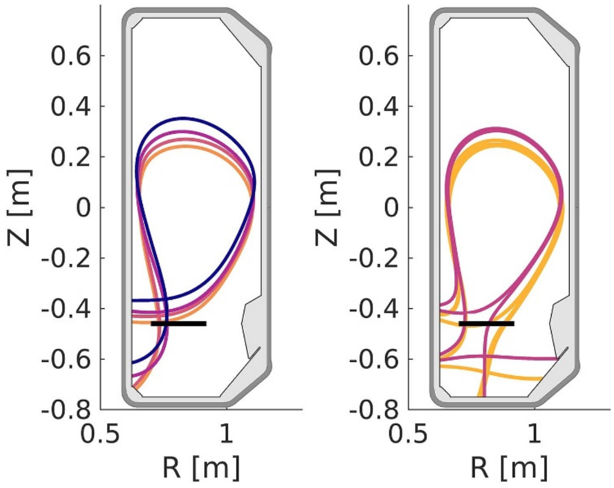

Figure 1. Schematic illustrating the vertically fixed probe plunge path (black line) during SN discharges (left) and SF discharges (right) at different plasma vertical positions indicated by the different separatrices colors.

care taken to keep the plasma volume constant. This allowed a fast reciprocating probe to sample different divertor regions, covering various vertical separations between the probe and the XPT. Figure 1 illustrates various SN and SF plasma discharges at different vertical heights with the fast probe shown as the fixed vertical black line. To minimize variations in divertor geometry and connection length $L_{\parallel}$, the inner and outer strike points were placed on vertical or near-vertical surfaces wherever possible.

This study examines four divertor configurations: (1) a low-density SN, (2) a low-density low-field side SF-minus, (3) a high-density SN, and (4) a high-density low-field side SF-minus. The low-field side SF-minus denomination means that the secondary XPT is located in the common region on the low-field side (as opposed to the high-field side or the private region). In the remainder of this article, the SF will specifically refer to the low-field side SF-minus. The separation between the primary and secondary separatrices of the SF, measured at the midplane (dR_{x2}), was 6 ± 2 mm for most of the discharges. One of the high-density SF discharges had a larger $dR_{x2} \approx 10 \pm 2$ mm, but this had no noticeable effect on the measured radial profiles at the probe position ~ 9 cm below the primary XPT. The low-density scenarios were conducted with $I_p = -240 \pm 10$ kA and $I_p = -255 \pm 5$ kA, while the high-density scenarios were performed with $I_p = -255 \pm 5$ kA.

The shots are divided into five groups: two for the low-density SN (having two slightly different plasma currents and line average densities and with the corresponding discharges taken in two separate campaigns, one in the summer of 2020 and the other in November–December 2022), and one for each of the low density SF, high density SN and high density SF. The TCV discharges used in this study are listed in table 1.

All attached low-density SN and SF discharges had an ohmic input power of $P_{\mathrm{ohm}} = 0.25$ MW while the high-density SN and SF discharges had $P_{\mathrm{ohm}} = 0.35$ MW. The electron density n_e to Greenwald density limit n_g ratio for the attached discharges was $n_e/n_g \approx 0.25 - 0.3$ while the high-density SN and SF discharges reached $n_e/n_g \approx 0.65$. The main plasma parameters are summarized in table 2, with Λ_{XPT} the normalized collisionality computed using $L_{\parallel}^{\mathrm{XPT}}$, the connection length to the outer target in the vicinity of the XPT, and plasma conditions measured at the probe position in the divertor. Λ_{XPT} is obtained by:

$$\Lambda_{\mathrm{XPT}} = \frac{\nu_{\mathrm{ei}} L_{\parallel}^{\mathrm{XPT}}}{\Omega_e \rho_s} \approx 9.647 \times 10^{-19} \frac{n_e \left[\mathrm{m}^{-3}\right] L_{\parallel}^{\mathrm{XPT}} \left[\mathrm{m}\right]}{\left(T_e \left[\mathrm{eV}\right]\right)^2}, \qquad (1)$$

where ν_{ei} is the electron–ion collision frequency, Ω_e is the electron gyrofrequency and ρ_s is the ion gyroradius. While this normalized collisionality can be used in the study of turbulent regimes [34], it is shown here for comparison purposes between SN and SF configurations and attached and detachment onset divertors. Λ_{XPT} increases substantially from attached to onset of detachment scenarios, and is about 2.5 times higher in the SF configurations than in the SN.

2.2. Diagnostic setup

The primary diagnostic tool used is the fast reciprocating probe [41], deployed at a lower horizontal port at $Z = -46$ cm. Designed for turbulence studies, the probe features ten electrodes (see legend of figure 2) that allow measuring of a wide range of plasma parameters, with measurement bandwidths up to 10 MHz for ion saturation current (I_{SAT}) and floating potential (V_f) fluctuations. The electron temperature (T_e) was measured using two of the probe tips as a swept double probe, applying a ± 300 V triangular wave at 1 kHz. The electron density n_e and its fluctuations ($\tilde{n}_e$) were inferred from the ion saturation current using the I_{SAT} electrode biased at -400 V. In doing so, the 1 ms time-resolved T_e is used. Therefore, temperature fluctuations above 1 kHz, which effect is typically under 20% [42], are neglected. During a given discharge, the probe performs at most two plunges, one per divertor configuration (SN and SF). The probe translation speed is approximately 1 mm ms^{-1}, and a full in–out stroke lasts ∼200 ms. Since the probe typically starts outside the plasma, the effective exposure time is shorter. Each probe trace shown in this study (for a given discharge and plasma scenario) corresponds to a single reciprocating-probe stroke, with only the inward leg used in the analysis.

The fluctuating electric field $\tilde{E}_Z$ is estimated using the V_f electrodes, located above and below the I_{SAT} electrode. For most flux surfaces, $E_Z \approx E_\theta$, with θ denoting the poloidal coordinate. This allows for determining the radial turbulent particle flux $\tilde{\Gamma}_r$ from $\tilde{E}_\theta$, the density fluctuation $\tilde{n}_e$ and the $\tilde{n}_e -$

Table 1. TCV plasma discharges used in this study.

	Attached		Detachment onset	
	SN & SF ($I_p = -240$ kA)	SN ($I_p = -255$ kA)	SN ($I_p = -255$ kA)	SF ($I_p = -255$ kA)
Discharges shot numbers	66 841	77 117	77 116	77 163
	66 844	77 118	77 121	77 167
	67 312	77 119	77 124	77 170
		77 123	77 163	77 172
			77 168	
			77 172	

Table 2. Plasma parameters of the different divertor configurations.

	Divertor geometry	Number of discharges	P_{ohm} [MW]	I_p [kA]	B_ϕ [T]	Line average n_e $[\mathrm{m}^{-3}]$	n_e/n_g	Λ_{XPT}
Attached	SN	3	0.25	−240	−1.44	$\approx 3.6 \times 10^{19}$	≈0.3	0.06 – 0.2
	SN	4	0.25	−255	−1.44	$\approx 3.1 \times 10^{19}$	≈0.25	0.04 – 0.2
	SF	3	0.25	−240	−1.44	$\approx 3.6 \times 10^{19}$	≈0.3	0.15 – 0.55
Detachment onset	SN	6	0.35	−255	−1.44	$\approx 8.4 \times 10^{19}$	≈0.65	0.4 – 8
	SF	4	0.35	−255	−1.44	$\approx 8.4 \times 10^{19}$	≈0.65	2 – 20

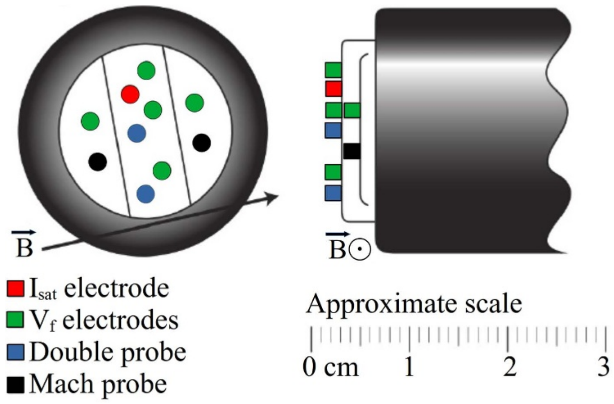

Figure 2. Schematic of the fast reciprocating probe head.

$\tilde{E}_\theta$ coherence $\gamma_{\tilde{n}_e\tilde{E}_\theta}$ and cross-phase angle δ from [43, 44]:

$$\tilde{\Gamma}_r\left[\mathrm{m}^{-2}\,\mathrm{s}^{-1}\right] = \frac{\langle \tilde{n}_e \tilde{E}_\theta \rangle}{B_\phi} = \frac{\langle \tilde{n}_e^2 \rangle^{1/2} \langle \tilde{E}_\theta^2 \rangle^{1/2}}{B_\phi} \gamma_{\tilde{n}_e\tilde{E}_\theta} \cos\delta. \quad (2)$$

The angled brackets in equation (2) denote ensemble averaging, and $\langle \tilde{n}_e^2 \rangle^{1/2}$ and $\langle \tilde{E}_\theta^2 \rangle^{1/2}$ are the absolute root mean square (RMS) levels of $\tilde{n}_e$ and $\tilde{E}_\theta$, written in the remainder of this work as $\tilde{n}_e^{\mathrm{RMS}}$ and $\tilde{E}_\theta^{\mathrm{RMS}}$. An ensemble averaging of 2 ms was used to calculate the RMS values with enough statistics. Given the probe translation speed, this time window results in a spatial resolution in absolute R-coordinate at the probe of ≈2 mm in the far SOL at the start of the plunge and ≈3.5 mm near the separatrix where the probe slows down as it approaches its deepest position. The radial turbulent convective heat flux is then obtained from $\tilde{\Gamma}_r$ as:

$$\tilde{Q}_r^{\mathrm{conv}}\left[\mathrm{W\,m}^{-2}\right] = \frac{5}{2} T_e \tilde{\Gamma}_r. \quad (3)$$

The radial and poloidal particle fluxes driven by DC $E \times B$ forces are respectively obtained as:

$$\Gamma_r^{E\times B}\left[\mathrm{m}^{-2}\,\mathrm{s}^{-1}\right] = n_e \frac{E_\theta B_\phi}{B^2} \quad (4)$$

and

$$\Gamma_\theta^{E\times B}\left[\mathrm{m}^{-2}\,\mathrm{s}^{-1}\right] = -n_e \frac{E_r B_\phi}{B^2}, \quad (5)$$

where B is the total magnetic field strength. The DC $E \times B$ radial and poloidal heat fluxes, $Q_r^{E\times B}$ and $Q_\theta^{E\times B}$, are obtained as:

$$Q_{r,\theta}^{E\times B}\left[\mathrm{W\,m}^{-2}\right] = 5 T_e \Gamma_{r,\theta}^{E\times B}, \quad (6)$$

where the electron and ion temperatures are assumed identical ($T_e = T_i$).

The plasma potential V_p, whose gradient determines E_θ and E_r, is calculated from V_f and T_e as:

$$V_p = V_f + 3T_e. \quad (7)$$

Two of the probe electrodes are used in a Mach tip configuration (see figure 2) and the parallel Mach number $M_\parallel$ is obtained using well established interpretation by theory [45, 46]. From $M_\parallel$, the parallel plasma fluid velocity $v_\parallel$ is obtained as:

$$v_\parallel = M_\parallel \times c_s, \quad (8)$$

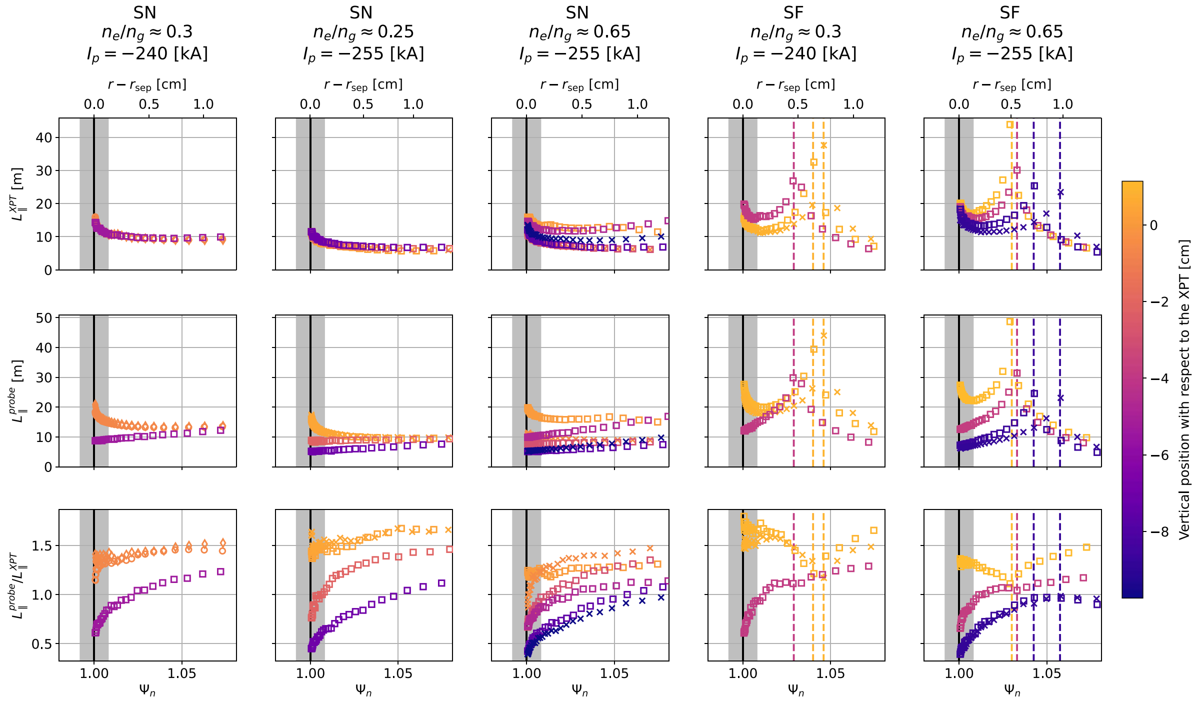

Figure 3. Profiles of $L_\parallel^{\rm XPT}$ (top row), $L_\parallel^{\rm probe}$ (middle row) and $L_\parallel^{\rm probe}/L_\parallel^{\rm XPT}$ (bottom row) for the different plunges across the divertor in all studied configurations. The colorbar indicates the average vertical position of the probe with respect to the XPT, progressing from deep blue for plunges far away from the XPT to yellow for plunges close to the XPT. The vertical black line and shaded gray region indicate the separatrix location and its uncertainty from magnetic reconstruction. The colored vertical dashed lines indicate the location of the secondary separatrix of the SF discharges.

where $c_{\rm s}$ is the ion sound speed. The parallel heat flux $q_\parallel$ to the divertor target can then be obtained as [47]:

$$q_\parallel \left[{\rm W\,m^{-2}}\right] = -\kappa T_{\rm e}^{\frac{5}{2}} \frac{\partial T_{\rm e}}{\partial s} + n_{\rm e} v_\parallel \left[\frac{5}{2}\left(T_{\rm e} + T_{\rm i}\right) + \frac{1}{2} m_{\rm i} v_\parallel^2 + I_0\right], \tag{9}$$

where κ is the parallel electron thermal conductivity $m_{\rm i}$ is the ion mass, I_0 is the atomic ionization and molecular potential, and $\partial/\partial s$ is the gradient along the field line s.

3. Normalization to $L_\parallel^{\rm XPT}$

The distance to the floor varies from shot to shot as the plasma is vertically displaced to scan the divertor region. This displacement alters the connection length from the XPT to the target, $L_\parallel^{\rm XPT}$, even for otherwise identical shots. While the connection length at the XPT is strictly speaking infinite, $L_\parallel^{\rm XPT}$ is taken from the point of lowest magnetic field strength near the XPT, along traced field lines. Any offset of this reference location from the nominal XPT is limited by the 5 mm × 6 mm grid resolution of the LIUQE equilibrium [48] and is negligible compared to the parallel connection lengths considered here. The position of TCV plasmas can also oscillate during a shot, causing the XPT to shift by several millimeters as the probe plunges. Therefore, rather than using the vertical distance between the probe and the XPT, we use the ratio $L_\parallel^{\rm probe}/L_\parallel^{\rm XPT}$ as a more robust and meaningful basis for cross-shot comparisons. There, $L_\parallel^{\rm probe}$ is the connection length from the probe tip, and both $L_\parallel^{\rm probe}$ and $L_\parallel^{\rm XPT}$ are obtained with respect to the outer target. The normalization effectively removes shot-to-shot variations in absolute geometry and provides a dimensionless metric of the relative position of the probe along the magnetic field line, with respect to the XPT. Connection lengths are calculated every 1 ms, with $L_\parallel^{\rm probe}$ evaluated at the probe tip as it traverses the plasma, and the corresponding values of $L_\parallel^{\rm XPT}$ are taken from the same field lines intersecting the probe trajectories.

Figure 3 shows the ratio $L_\parallel^{\rm probe}/L_\parallel^{\rm XPT}$ against the normalized poloidal flux coordinate $\psi_{\rm n}$. For reference, the corresponding distance from the separatrix projected at the outer midplane, $r - r_{\rm sep}$, is also shown. The color bar in figure 3 indicates the average vertical position of the probe relative to the XPT, with colors ranging from deep blue at the farthest positions to yellow at the closest. The vertical black line denotes the separatrix position, and the shaded region around it indicates the uncertainty from magnetic reconstruction. The secondary separatrix of the SF discharges are indicated with vertical dashed lines having the same color of the corresponding probe plunge. While $L_\parallel^{\rm XPT}$ and $L_\parallel^{\rm probe}$ do not always follow a monotonic trend with vertical plasma shifts, the ratio $L_\parallel^{\rm probe}/L_\parallel^{\rm XPT}$ does. Higher

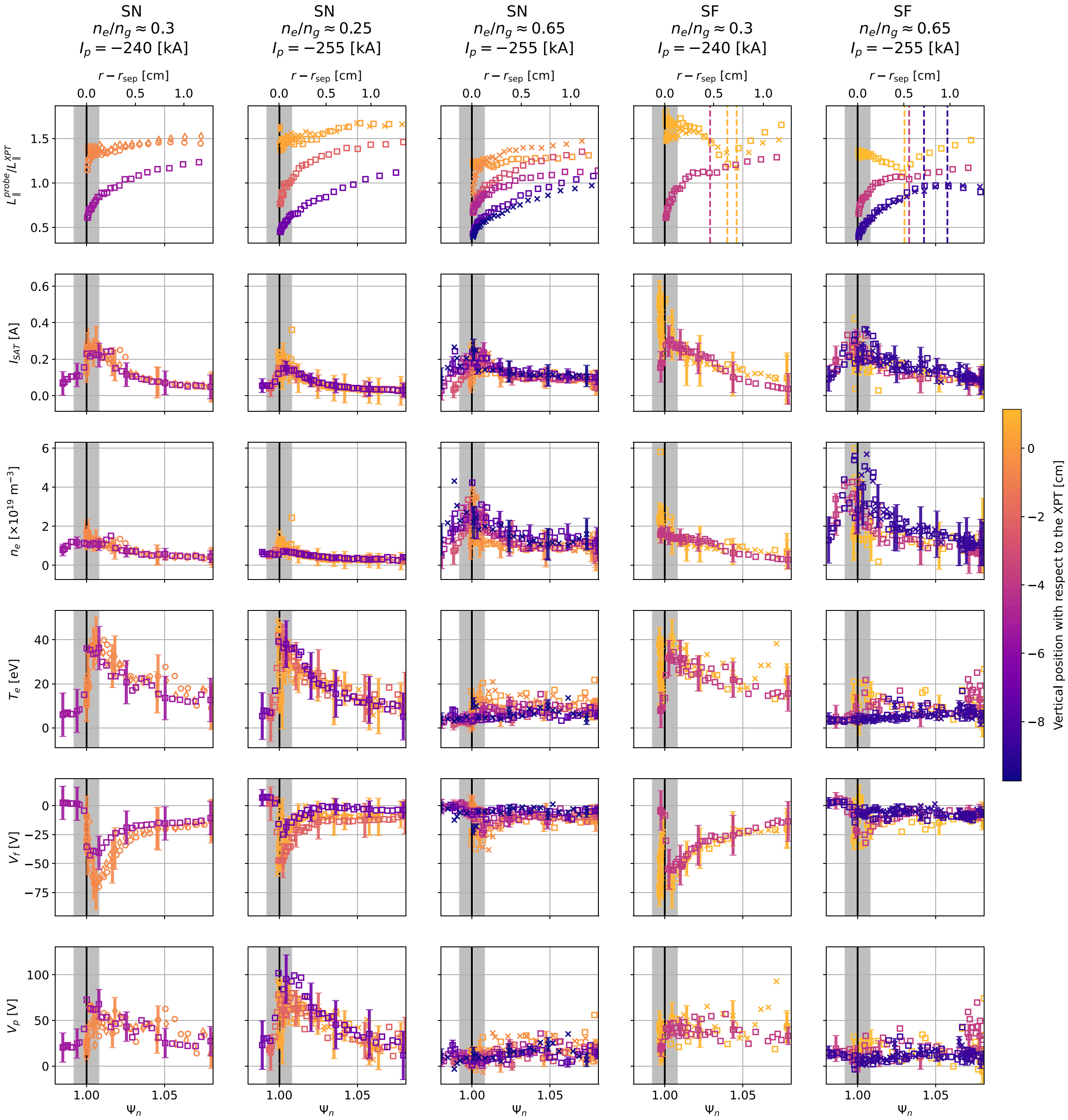

Figure 4. Mean radial profiles of I_{SAT} (second row), n_{e} (third row), T_{e} (fourth row), V_{f} (fifth row) and V_{p} (sixth row) for all probe plunges. The $L_{\parallel}^{\mathrm{probe}}/L_{\parallel}^{\mathrm{XPT}}$ ratio is shown in the first row. The colorbar progresses from deep blue for plunges far away from the XPT to yellow for plunges close to the XPT. The errorbars represent one standard deviation. The vertical black line and shaded gray region indicate the separatrix location and its uncertainty from magnetic reconstruction. The colored vertical dashed lines (shown in the first row only) indicate the location of the secondary separatrix of the SF discharges.

values correspond to plunges nearer to the XPT, while lower values are observed deeper in the divertor. For the SF shots, plunges near the XPT exhibit a distinct drop in this ratio at the secondary separatrix of the SF configuration, followed by an increase approaching the separatrix.

4. Mean profiles

The mean divertor profiles across SN and SF configurations show increasing electron density toward the divertor floor and flattening electron temperature as the plasma transitions from attached to near-detached conditions. SF discharges show higher n_{e} and I_{SAT} than SN under comparable conditions, with similar or slightly lower T_{e}. The density decay length λ_{n} increases near the XPT at the detachment onset in both SN and SF divertors. Profiles of V_{f} display well-shaped minima near the separatrix in attached cases, which progressively flatten at the detachment onset and closer to the floor. Despite variation in V_{f} and T_{e}, the resulting plasma potential V_{p} remains approximately constant across the divertor. The sheath current imbalance factor Δ, which quantifies deviations from ambipolar current closure at the sheath, is found to be large and increase near the separatrix at the detachment onset.

Figure 4 presents radial profiles of I_{SAT}, n_e, T_e, V_f, and V_p together with the ratio $L_{\parallel}^{\rm probe}/L_{\parallel}^{\rm XPT}$. Despite the increase in n_e towards the floor at the detachment onset, the I_{SAT} amplitude varies little between the low n_e/n_g and $n_e/n_g \approx 0.65$ scenarios, indicating that full detachment is not attained. Following the criteria outlined in [4, 18], the definition adopted in this work describes the detachment onset as a divertor with low T_e (< 10 eV) and increased n_e towards the divertor floor compared to attached conditions, accompanied by a flattening of the I_{SAT} profiles, though with no reduction in amplitude. At the detachment onset, all probe plunges show a significant T_e reduction extending up to the XPT. The decrease is less pronounced near the XPT but remains about 50% lower than in attached conditions. We define the *dissipative region* as the divertor volume below the XPT, where T_e drops to around 5 eV.

Across all regimes, SF divertors exhibit higher I_{SAT} and n_e at the separatrix compared to SN divertors, while T_e remains similar between configurations. In attached conditions, I_{SAT} in SF divertors exceeds that in SN divertors by 30%–50%, depending on plasma current. At the onset of detachment, I_{SAT} increases by 15%–20% in both configurations relative to their respective attached states. The separatrix n_e roughly triples as detachment is approached, maintaining a higher value in the SF divertors. In contrast, T_e drops significantly across all configurations at the onset of detachment, from about 40 eV to $15-20$ eV in the plunges closest to the XPT and further to $5-10$ eV in the rest of the divertor volume. Because of the noticeable difference in I_{SAT} and n_e between the two SN attached scenarios, and since their discharges were recorded in separate experimental campaigns under distinct operational conditions, these cases are treated separately throughout this work.

In the attached scenarios, a distinct peak in the I_{SAT} and n_e profiles is observed at the separatrix in the plunges closest to the XPT, especially visible in the SF configuration. This feature may arise from physical phenomena intrinsic to the XPT, or it may indicate that the probe is entering the core plasma just above the XPT. The grid resolution used in the LIUQE magnetic reconstruction for TCV is of 5 mm × 6 mm. Owing to the use of simplified basis functions, the absence of internal measurements and magnetic measurement uncertainties, the precise location of the XPT may not be known to millimeter accuracy, introducing the possibility that the probe crosses into the core in this region. Nonetheless, core physics are unlikely to explain this rise in n_e and I_{SAT}. The observed behavior is indeed consistent with previous measurements at the DIII-D XPT [25, 26], where the observed electron pressure peak was attributed to strong ionization rates producing cold ions, a low ion pressure P_i, and an elevated electron pressure P_e to maintain total pressure balance. A detailed investigation of these profile peaks near the XPT is beyond the scope of this work and is deferred to future studies.

The I_{SAT} and n_e profiles are seen to peak at the separatrix and decay towards the far SOL with a sharp drop in the private-flux region (PFR). The n_e profiles feature the formation of a shoulder region, especially apparent in the SN scenarios at the detachment onset. Figure 5 plots the decay lengths λ_n and λ_T versus the average vertical distance from the XPT. Decay lengths values are capped at 10 cm with larger values indicating flat profiles. A double exponential was used to fit the n_e profiles in the near and far SOL whereas only a single exponential was needed for the T_e profiles. In the near SOL, λ_n is comparable for both SN and SF configurations under attached conditions at ≈1 cm. In the far SOL λ_n increases by a factor of $2-3$. At the onset of detachment, a local rise to $\lambda_n \approx 4$ cm (SN) and ≈5.5 cm (SF) is produced in the plunge nearest the XPT in the near SOL. This rise does not propagate to plunges further away from the XPT in the divertor, but results in a flat n_e profiles in the far SOL of the SN configuration ($\lambda_n \geqslant 10$ cm in figure 5). This behavior will be shown later on to be due to turbulent spreading above the dissipative region. The temperature scale length is found to be comparable or slightly larger in the SF than in the SN configurations under attached conditions, and effectively becomes infinite at the detachment onset for all plunges except those closest to the XPT.

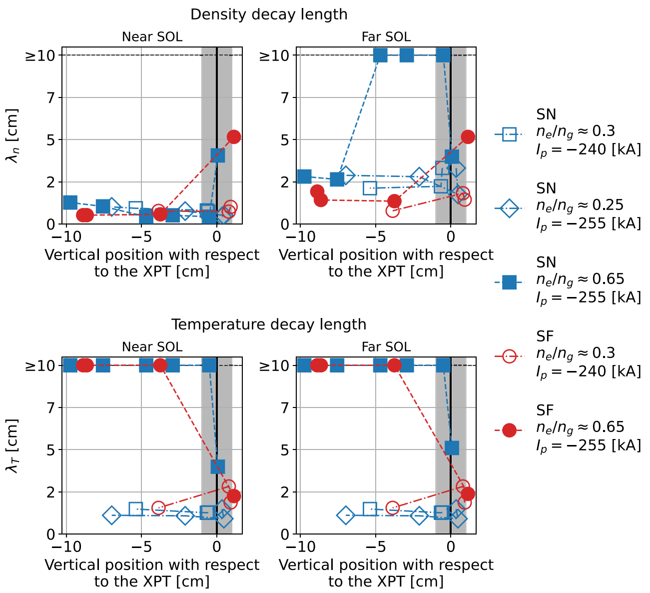

Figure 5. Density (first row) and temperature (second row) decay lengths in the near SOL (left column) and far SOL (right column) for the different divertor configurations plotted against the average vertical position relative to the XPT. Blue and red markers represent SN and SF divertors respectively; empty and filled markers represent attached and near-detached condition respectively.

Potential profiles and sheath current imbalance

A collapse of the V_p profiles can be seen across the studied configurations, especially in the onset of detachment scenarios and in the attached SF where they also flatten. This behavior results from the combined evolution of the floating potential V_f and the electron temperature T_e. As V_f is directly measured from the probe, it provides the most reliable indication of how local current balance evolves in the divertor, and hence of the mechanisms shaping V_p.

In the attached scenarios, V_f decreases near the separatrix, forming negative wells that deepen for plunges closer to the XPT. This behavior, previously reported in [49], is attributed to the interaction between turbulence-driven polarization currents and poloidally asymmetric diamagnetic currents [50]. The imbalance between these currents, which push charged particles radially outward, creates the observed V_f structure. A negative V_f indicates that excess electrons are evacuated through the sheath together with a radially outward ion current, while a positive V_f occurs when ions are lost through the sheath with a radially outward electron current. When the parallel ion and electron currents are balanced, V_f goes to zero.

At the detachment onset, the negative V_f wells become shallower and flatten completely in the deepest plunges near the divertor floor, indicating that the parallel currents approach balance. As a result, the need for radial current closure vanishes, and the associated radial electric fields are no longer sustained. The observed flattening of V_f, combined with the reduced T_e, suggests that the usual approximation $V_\mathrm{p} \approx 3T_\mathrm{e}$ becomes increasingly valid as V_f tends to zero near detachment, whereas in attached divertors, accounting for V_f and plasma currents is essential to accurately determine V_p.

In contrast to V_f, T_e increases toward the separatrix in attached cases, partially compensating the V_f variation and producing a relatively poloidally uniform V_p across the divertor. At the detachment onset, in both SN and SF configurations, a similar compensation between V_f and T_e occurs near the XPT, while both quantities flatten toward the floor. The resulting collapse of V_p leaves minimal vertical variation and no significant potential drop within experimental uncertainty.

The sheath current imbalance, defined as $\Delta = \exp(-V_\mathrm{f}/T_\mathrm{e}) - 1$ [50], is computed from the measured V_f and T_e. Δ is a dimensionless measure of the local sheath current imbalance: $\Delta > 0$ corresponds to a local excess of electron current relative to the sheath ion current, while $\Delta < 0$ indicates a relative ion current excess. In attached SN and SF divertors, Δ ranges between 1 and 5 in the near SOL, peaking near the separatrix with higher values for plunges closer to the XPT. At the detachment onset, Δ reaches up to 10 at the separatrix for all plunges. These large Δ values denote strong deviations from ambipolarity and enhanced perpendicular current contributions. As detachment progresses, the poloidal dependence of Δ largely disappears and all plunges show a similar separatrix peak. The non-ambipolar current demand thus becomes localized to the separatrix and shared along connected field lines, producing a flux-surface offset in V_p rather than a large poloidal gradient. This explains the coexistence of high Δ values with flattened V_p profiles in the SOL.

The diamagnetic and polarization components of Δ follow the model of Loizu *et al* [50]:

$$\Delta = 2\pi q \left[\frac{1}{k_\theta \rho_\mathrm{s}} \frac{2}{5} \left(\frac{\rho_\mathrm{s}}{L_\mathrm{p}} \right)^2 - 2\frac{\delta P}{P} \left(\frac{\rho_\mathrm{s}}{L_\mathrm{p}} \right) \right], \qquad (10)$$

where the first term represents the polarization current contribution and the second the diamagnetic contribution, with q the safety factor, k_θ the poloidal wavenumber, ρ_s the ion sound gyroradius, L_p the pressure gradient scale length, and $\delta P/P$ the normalized pressure modulation along the field line. The inferred $k_\theta \rho_\mathrm{s}$ values are 10^{-3}–10^{-2} in attached conditions and decrease to $\sim 10^{-3}$ near detachment, implying that large-scale, fluid-like structures persist even as the V_f and V_p profiles flatten.

5. Turbulence measurements

5.1. Fluctuation magnitudes

The absolute RMS levels of $\tilde{I}_\mathrm{SAT}$, $\tilde{E}_\theta$ and $\tilde{V}_\mathrm{f}$ (respectively the I_SAT, E_θ, and V_f fluctuations), denoted $\tilde{I}_\mathrm{SAT}^\mathrm{RMS}$, $\tilde{E}_\theta^\mathrm{RMS}$, and $\tilde{V}_\mathrm{f}^\mathrm{RMS}$, are shown in figure 6 for both SN and SF divertors. Fluctuation amplitudes generally increase with distance from the divertor floor, exhibiting a maximum in the region sampled closest to the XPT across all divertor configurations, and falling off in the PFR. This trend is particularly evident in the attached scenarios, whereas the RMS levels flatten and collapse at the onset of detachment.

In both SN and SF divertors, $\tilde{I}_\mathrm{SAT}^\mathrm{RMS}$ is relatively flat closer to the divertor floor and increases as it approaches the XPT, especially near the separatrix. Near-detached plasmas exhibit slightly higher $\tilde{I}_\mathrm{SAT}^\mathrm{RMS}$ levels compared to attached conditions. No clear difference is observed between SN and SF configurations despite difference in geometry and higher Λ_XPT in the SF divertors. For the $\tilde{E}_\theta$ and $\tilde{V}_\mathrm{f}$ fluctuations, their RMS profiles vary clearly with vertical position in attached divertors but collapse across plunges at the detachment onset with overall lower magnitudes. Only plunges nearest the XPT retain elevated RMS values, with maxima located near the separatrix.

A sharp drop in the RMS profiles is observed across the separatrix into the PFR in attached discharges, particularly near the XPT. In near-detached conditions with $n_\mathrm{e}/n_\mathrm{g} \approx 0.65$, the steep gradient persists only in plunges closest to the XPT, while the profile flattens in all others, indicating smoother radial variation. Although the RMS amplitudes of $\tilde{E}_\theta$ and $\tilde{V}_\mathrm{f}$ decrease at the detachment onset, the flatter profiles are consistent with faster radial propagation of turbulent structures. As demonstrated theoretically [33, 34], higher Λ_XPT increases blob velocities and turbulence spreading. The observed broadening of the RMS profiles supports enhanced turbulent transport at higher Λ_XPT without requiring increased fluctuation amplitude.

5.2. Turbulent fluxes

As the broadening of particle and heat flux profiles is a key objective of detachment, it is essential to examine the role of turbulent fluxes as potential contributors. The flattening of fluctuation levels already hints at larger radial turbulent transport at the detachment onset. The turbulent particle flux $\widetilde{\Gamma}_r$ is seen to increase near the XPT and upstream of the dissipative region in both near-detached SN and SF configurations, while remaining largely unchanged elsewhere in the divertor. The

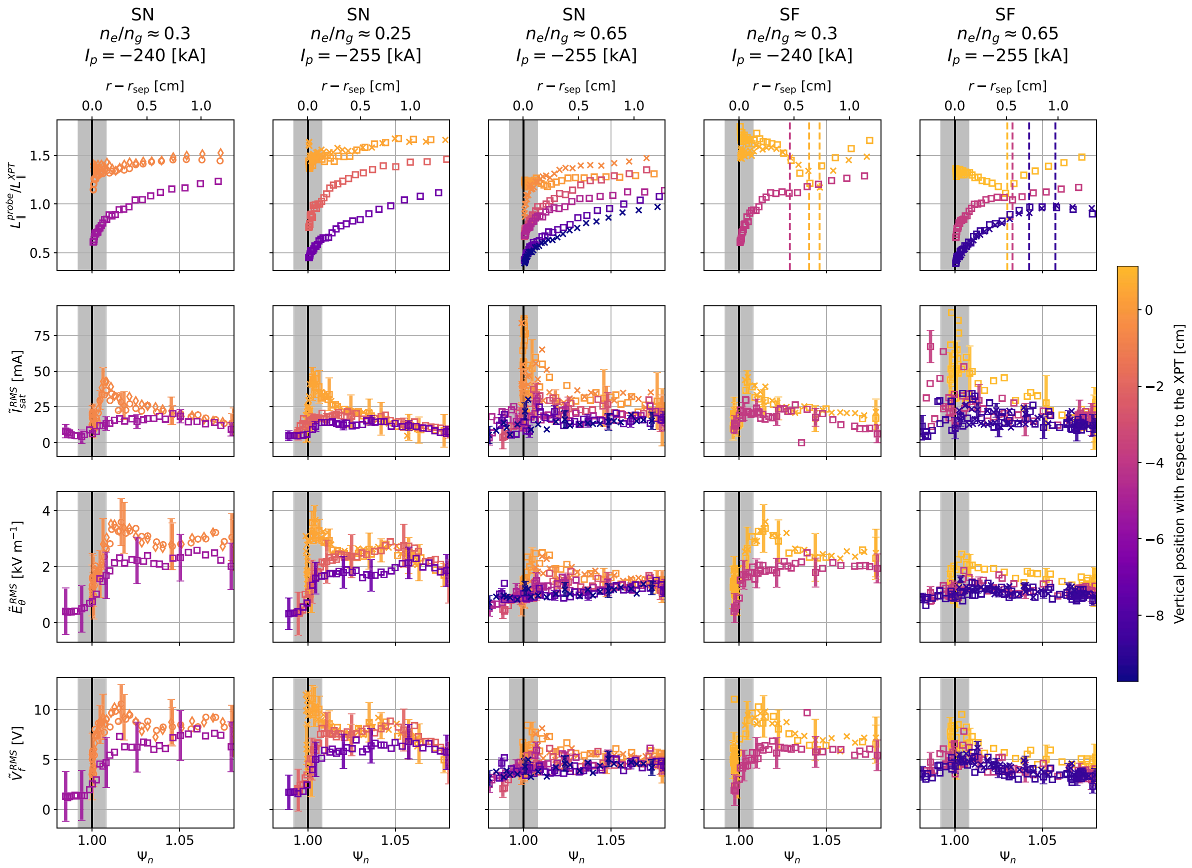

Figure 6. Radial profiles of the RMS levels of $\tilde{I}_{\mathrm{SAT}}$ (second row), $\tilde{E}_\theta$ (third row) and $\tilde{V}_{\mathrm{f}}$ (fourth row). The colorbar progresses from deep blue for plunges far away from the XPT to yellow for plunges close to the XPT. The errorbars represent one standard deviation. The vertical black line and shaded gray region indicate the separatrix location and its uncertainty from magnetic reconstruction. The colored vertical dashed lines (shown in the first row only) indicate the location of the secondary separatrix of the SF discharges.

flattening of density profiles near the XPT can be attributed to this $\widetilde{\Gamma}_r$ enhancement. Turbulent heat fluxes $\widetilde{Q}_{\mathrm{r}}^{\mathrm{conv}}$ are found to be higher in SF than in SN divertors in attached conditions and to decrease and flatten near detachment in both configurations, especially closer to the divertor floor.

Figure 7 presents the profiles of the correlation coefficient $\gamma_{\tilde{n}_e\tilde{E}_Z}\cos\delta$ and the turbulent radial particle and convective heat fluxes, $\widetilde{\Gamma}_{\mathrm{r}}$ and $\widetilde{Q}_{\mathrm{r}}^{\mathrm{conv}}$, for the studied SN and SF divertors. In attached plasmas, the correlation coefficient increases towards the divertor floor, while it decreases at the detachment onset. This reversed trend offsets the increase in $\widetilde{I}_{\mathrm{SAT}}$, yielding similar $\widetilde{\Gamma}_{\mathrm{r}}$ away from the XPT in both attached and near-detached conditions.

Despite the higher Λ_{XPT} in SF divertors, no increase in $\widetilde{\Gamma}_{\mathrm{r}}$ is seen compared to the equivalent SN divertors. In the attached SN divertor, $\widetilde{\Gamma}_{\mathrm{r}}$ remains around 1×10^{21} m^{-2}s^{-1}, or slightly lower, away from the XPT. This is comparable to $\widetilde{\Gamma}_{\mathrm{r}}$ in the attached SF configuration. Near the XPT, $\widetilde{\Gamma}_{\mathrm{r}}$ increases to $1-2 \times 10^{21}$ m^{-2}s^{-1} in both geometries. At the detachment onset, values within the dissipative region remain comparable to those in the attached cases, while closer to and above the XPT, $\widetilde{\Gamma}_{\mathrm{r}}$ increases by a factor of $2-4$, reaching $\sim 4 \times 10^{21}$ m^{-2}s^{-1}.

The onset of detachment is therefore accompanied by an enhancement of turbulent radial transport upstream of the dissipative region, with no significant change observed in the near-detached divertor volume. This rise in $\widetilde{\Gamma}_{\mathrm{r}}$ near and above the XPT aligns with the strong increase in λ_n observed in the same region. These two effects combined indicate that particles enter the divertor leg having been already radially spread out upstream. This can explain the observed flattening of density profiles without invoking additional transport mechanisms.

The turbulent convective heat flux $\widetilde{Q}_{\mathrm{r}}^{\mathrm{conv}}$ is higher in the attached SF ($\sim$5 kW m^{-2}) than in the attached SN ($\sim$3 kW m^{-2}) away from the XPT, with the same trend continuing in near-detached cases. This difference is most visible in plunges $\sim$5 cm below the XPT, while it vanishes in plunges closer to the floor where $\widetilde{Q}_{\mathrm{r}}^{\mathrm{conv}}$ drops and profiles flatten. At the detachment onset, both SN and SF divertors show reduced and flattened $\widetilde{Q}_{\mathrm{r}}^{\mathrm{conv}}$ profiles closer to the floor, consistent with the flattened T_{e} profiles and weak changes in $\widetilde{\Gamma}_{\mathrm{r}}$. In contrast to the turbulent particle fluxes, $\widetilde{Q}_{\mathrm{r}}^{\mathrm{conv}}$ in the vicinity of the XPT remains similar between attached and near-detached conditions in both geometries, peaking around 10 kW m^{-2} near the separatrix.

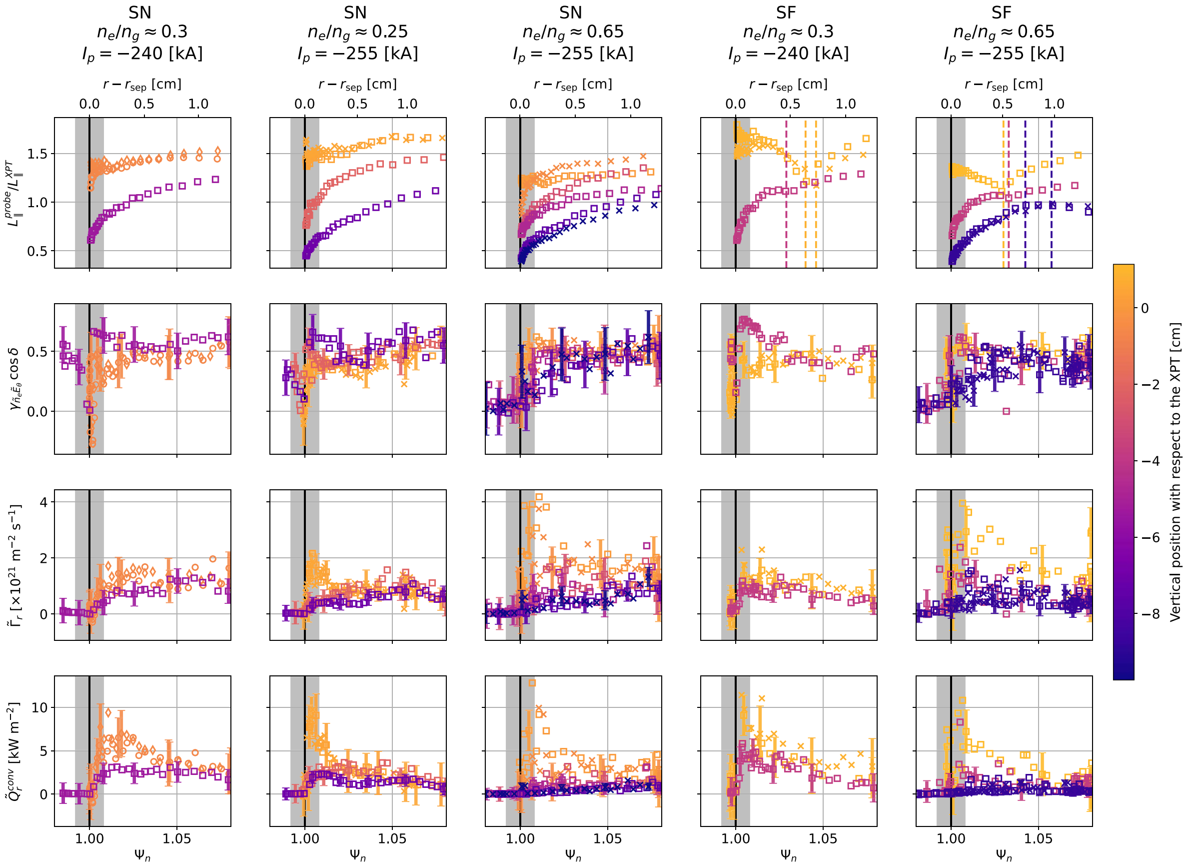

Figure 7. Radial profiles of $\gamma_{\tilde{n}_e\tilde{E}_Z} \cos\delta$ (second row), $\widetilde{\Gamma}_\mathrm{r}$ (third row) and $\widetilde{Q}_\mathrm{r}^\mathrm{conv}$ (fourth row). The colorbar progresses from deep blue for plunges far away from the XPT to yellow for plunges close to the XPT. The errorbars represent one standard deviation. The vertical black line and shaded gray region indicate the separatrix location and its uncertainty from magnetic reconstruction. The colored vertical dashed lines (shown in the first row only) indicate the location of the secondary separatrix of the SF discharges.

6. DC $E \times B$ flows in the divertor volume

6.1. Radial DC $E \times B$ flows

The radial DC $E \times B$ flows inferred from vertical gradients of the plasma potential V_p are only identified in one operational regime, the attached SN, where $\Gamma_\mathrm{r}^{E\times B}$ becomes comparable in magnitude to turbulent levels. In the attached SF and at the onset of detachment, the vertical invariance of V_p effectively reduces E_θ and the DC radial drifts within experimental errors.

The E_θ profiles, reconstructed radial DC particle fluxes $\Gamma_\mathrm{r}^{E\times B}$ and associated heat fluxes $Q_\mathrm{r}^{E\times B}$ are shown in figure 8. As seen in figure 4, in nearly all configurations, the V_p profiles are collapsed together, resulting in negligible electric fields E_θ and minimal radial DC transport. A well defined E_θ profile only appears in the attached SN configurations, with a plateau just outside the separatrix at 0.5 kV m^{-1} and resulting in $\Gamma_\mathrm{r}^{E\times B} \sim -2 \times 10^{21}$ m^{-2}s^{-1} in the near-SOL, on par with turbulent $\widetilde{\Gamma}_\mathrm{r}$ levels. The negative sign indicates the direction of $\Gamma_\mathrm{r}^{E\times B}$ from the SOL towards the PFR. The corresponding heat flux $Q_\mathrm{r}^{E\times B}$ reaches approximately -50 kW m^{-2}. Both $\Gamma_\mathrm{r}^{E\times B}$ and $Q_\mathrm{r}^{E\times B}$ magnitudes drop sharply across the separatrix into the PFR. In this configuration still, while the particle flux is comparable to $\widetilde{\Gamma}_\mathrm{r}$, the DC heat flux substantially exceeds $\widetilde{Q}_\mathrm{r}^\mathrm{conv}$ by a factor of $5-20$.

In the attached SF configuration, the large spread observed in the V_p profiles is attributed to the limited number of available plunges and to the strong magnetic flux expansion between the two nearby null points, which stretches spatial gradients and amplifies shot-to-shot variability. Nonetheless, the radial $E \times B$ fluxes display consistently positive values, suggesting that the radial drifts are pushing particles away from the separatrix in this configuration.

At the onset of detachment, the collapse and flattening of the V_p profiles strongly reduce E_θ and the associated radial DC $E \times B$ drifts. While the data exhibit significant scatter, particularly in the SF configuration, the radial DC $E \times B$ fluxes consistently show positive $\Gamma_\mathrm{r}^{E\times B}$ values, indicating that radial drifts are pushing particles and heat away from the separatrix. Because of the large scatter in the data, additional measurements would be required to further quantify this behavior. Importantly, no enhanced radial $E \times B$ transport is observed at the onset of detachment.

These results demonstrate that radial DC $E \times B$ transport is only significant in a narrow regime of attached SN plasmas with vertically varying V_p structures and gradients. As detachment sets in, the suppression of V_p gradients in the studied plasma discharges weakens this transport channel, leaving turbulent spreading above the dissipative region as the dominant and only observed enhanced mechanism for radial transport.

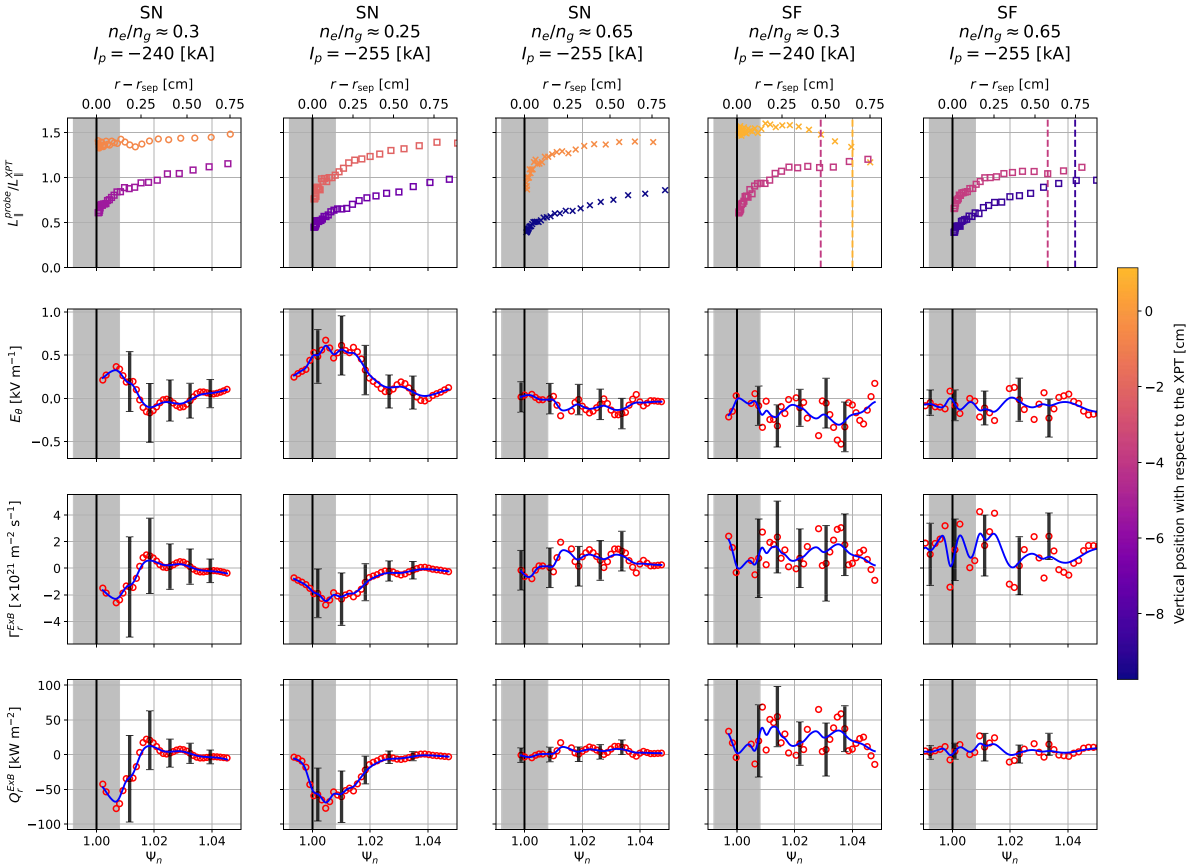

Figure 8. Radial profiles of E_θ (second row), $\Gamma_r^{E\times B}$ (third row) and $Q_r^{E\times B}$ (fourth row). The blue curve is a smooth fit through the interpolated data (red circles). The error bars are obtained from error propagation. The vertical black line and shaded gray region indicate the separatrix location and its uncertainty from magnetic reconstruction. The colored vertical dashed lines (shown in the first row only) indicate the location of the secondary separatrix of the SF discharges.

6.2. Poloidal DC $E\times B$ flows

The poloidal DC $E\times B$ transport is seen to dominate both particle and heat fluxes in the private flux region (PFR) across all attached SN and SF divertor configurations. In these cases, well-shaped profiles of the radial electric field E_r generate strong poloidal $E\times B$ flows at the separatrix inside the PFR that decay rapidly in the SOL. The SN configuration consistently exhibits stronger shear and larger E_r wells than the SF, but comparable $\Gamma_\theta^{E\times B}$ and $Q_\theta^{E\times B}$ magnitudes. At the onset of detachment, this structure is disrupted: the E_r well disappears and is replaced by a small positive hump in the PFR, while E_r gets suppressed in the SOL. As a result, poloidal $E\times B$ particle and heat fluxes reverse direction in the PFR and are suppressed in the SOL.

Figure 9 shows the E_r profiles alongside the poloidal DC $E\times B$ particle and heat fluxes. In attached SN divertors, E_r exhibits a deep well in the PFR just inside the separatrix, reaching minima between $-2.8\,\mathrm{kV\,m^{-1}}$ and $-4.4\,\mathrm{kV\,m^{-1}}$, while in the attached SF this well is shallower, reaching only $-1.2\,\mathrm{kV\,m^{-1}}$. At the onset of detachment, the E_r well disappears and a small positive hump emerges in the PFR, while E_r flattens in the SOL for both SN and SF cases, consistent with the suppression of V_p gradients near detachment.

The $\Gamma_\theta^{E\times B}$ and $Q_\theta^{E\times B}$ profiles follow the structure of E_r. In attached SN configurations, $\Gamma_\theta^{E\times B}$ exhibits a negative well inside the PFR with increasing depth toward the divertor floor around $-2\times10^{22}\,\mathrm{m^{-2}s^{-1}}$, and $Q_\theta^{E\times B}$ reaches a minima at $\sim-280\,\mathrm{kW\,m^{-2}}$. Both quantities are roughly a factor of two smaller in the attached SF, though the probe plunges do not go as close to the divertor floor as in the attached SN. The attached SN features a small positive $\Gamma_\theta^{E\times B}$ peak around $5\times10^{21}\,\mathrm{m^{-2}s^{-1}}$ and $Q_\theta^{E\times B}$ peak between 35 and $100\,\mathrm{kW\,m^{-2}}$ in the SOL, features which are absent from the attached SF where the SOL profiles are flatter. As detachment develops, the $\Gamma_\theta^{E\times B}$ and $Q_\theta^{E\times B}$ profiles reverse sign in the PFR, consistent with the appearance of the positive E_r hump, and are suppressed in the SOL, where the flattened potential profile eliminates the DC $E\times B$ drive.

Overall, DC poloidal $E\times B$ transport provides an important cross-field channel in the PFR during attached operation. At the detachment onset, with the collapse of E_r and V_p gradients, there is a transition to a regime where drift-driven transport weakens and inter-leg coupling is confined to the residual positive E_r feature inside the PFR and near the separatrix.

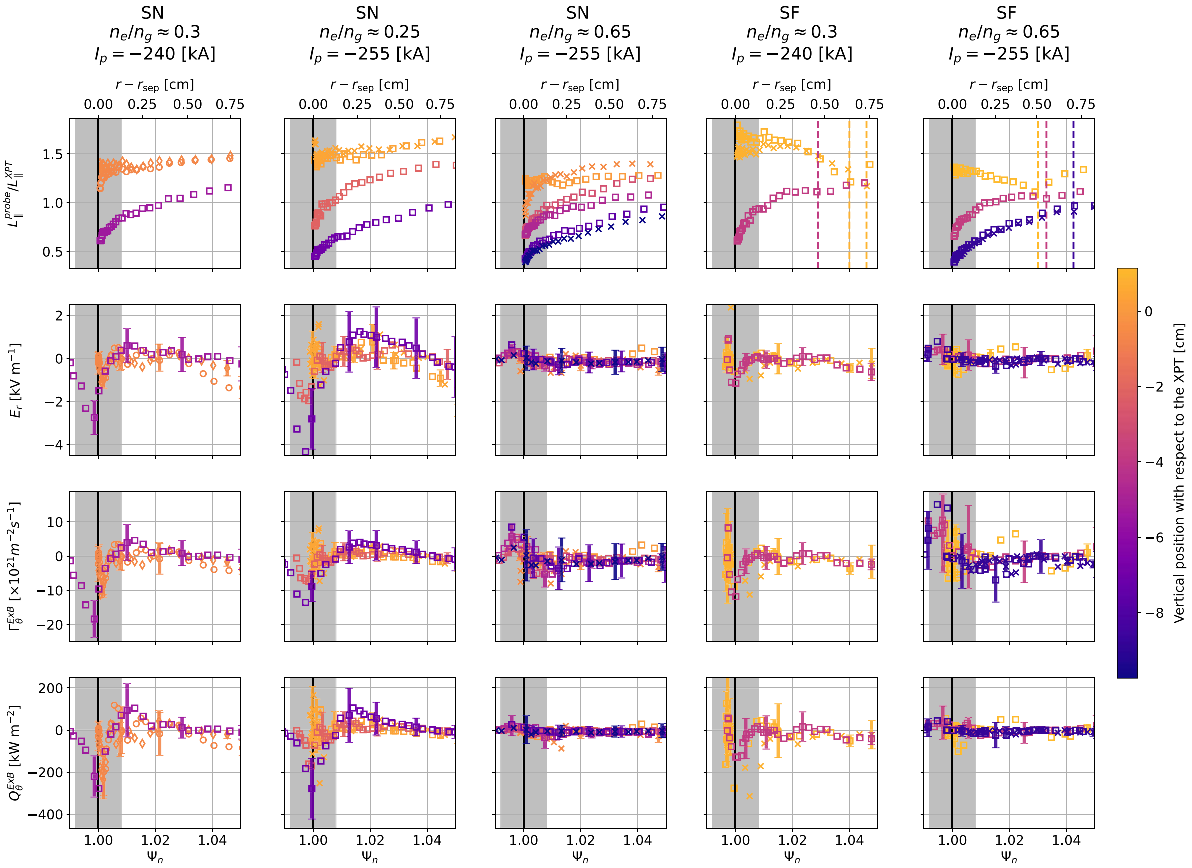

Figure 9. Radial profiles of E_r (second row), $\Gamma_\theta^{E\times B}$ (third row) and $Q_\theta^{E\times B}$ (fourth row). The colorbar progresses from deep blue for plunges far away from the XPT to yellow for plunges close to the XPT. The error bars represent one standard deviation of E_r and the uncertainty from error propagation in $\Gamma_\theta^{E\times B}$ and $Q_\theta^{E\times B}$. The vertical black line and shaded gray region indicate the separatrix location and its uncertainty from magnetic reconstruction. The colored vertical dashed lines (shown in the first row only) indicate the location of the secondary separatrix of the SF discharges.

7. Parallel transport

With the suppression of temperature gradients near detachment, convection is found to become the dominant mechanism for parallel heat transport. This is reflected in the broadening of the parallel velocity profiles at the detachment onset, indicating that the SOL divertor plasma begins to move as a bulk throughout the divertor.

The parallel heat flux $q_\parallel$ to the divertor target is given in equation (9). Its first term represents the conductive component of $q_\parallel$, $q_\parallel^{\text{cond}} = -\kappa T_e^{5/2}\partial T_e/\partial s$, while the second term represents the convective component, $q_\parallel^{\text{conv}} = n_e v_\parallel \left[\frac{5}{2}(T_e + T_i) + \frac{1}{2} m_i v_\parallel^2 + I_0\right]$.

Past studies have shown that conduction typically dominates $q_\parallel$ under attached conditions while convection takes over as the primary carrier of energy as the parallel temperature gradient weakens near detachment [51–53]. The behavior of the $v_\parallel$ and $M_\parallel$ profiles shown in figure 10 support an increased convection role at the detachment onset. In the attached SN divertor, $v_\parallel$ rises near the separatrix from about 10 km s^{-1} near the XPT to 35 km s^{-1} closer to the divertor floor, a trend followed by $M_\parallel$ (going from 0.2 near the XPT to 0.5 closer to the floor) and consistent with sheath theory [54]. At the detachment onset, the $v_\parallel$ profiles broaden substantially compared to the attached case and collapse together, in agreement with previous measurements of divertor plasma flows in DIII-D [55]. This is indicative that, at the detachment onset, convection drives the divertor SOL plasma to move more uniformly as a bulk. Despite $v_\parallel$ reaching only 20 km s^{-1} at the detachment onset at the separatrix, the higher $M_\parallel$ of 0.65 compared to the attached scenarios indicates that the SOL plasma moves at a larger fraction of the local sound speed, consistent with enhanced convective transport.

In the attached SF divertor, the profiles are broader than in the equivalent SN case, with lower $v_\parallel$ near the separatrix but higher values in the far SOL within the dissipative region. The plunge nearest the XPT shows a trend similar to that of the SN. The plunge below the XPT features significantly higher $v_\parallel$ in the far SOL, followed by a clear drop at the SF secondary separatrix before gradually rising toward the PFR. At the detachment onset, the SF profiles evolve in a manner similar to those in the SN divertor, but with little change in magnitude and without the distinct drop in $v_\parallel$. The broader profiles observed

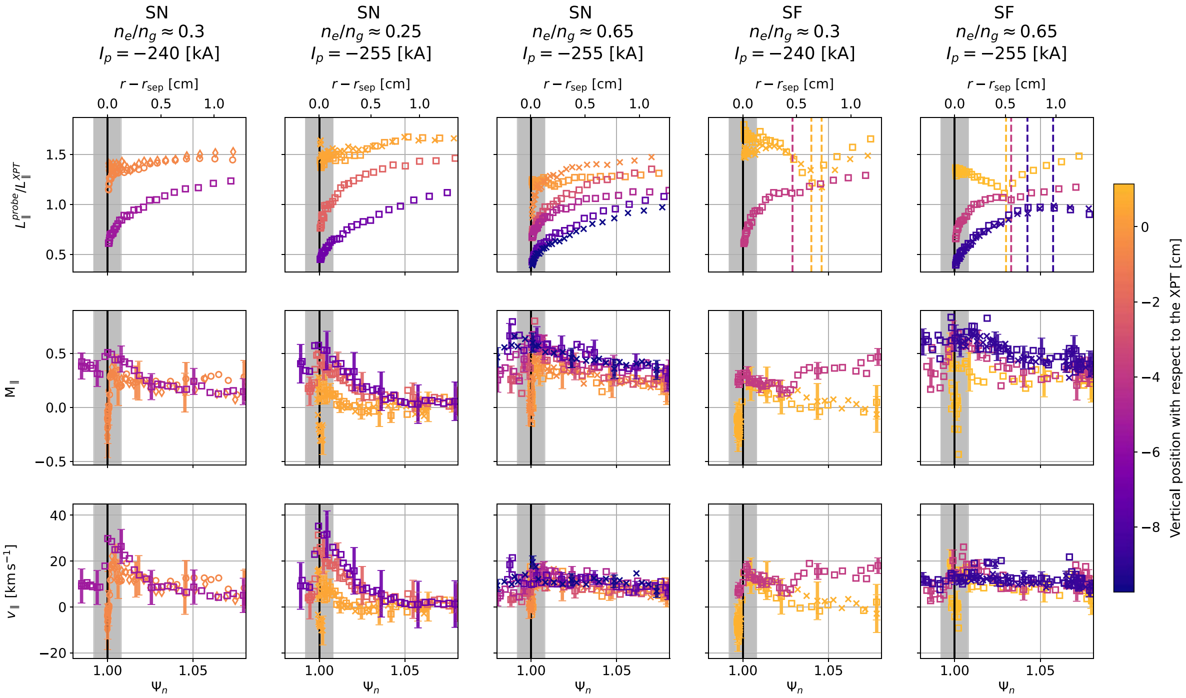

Figure 10. Radial profiles of $Ma_\parallel$ (second row) and $v_\parallel$ (third row). The colorbar progresses from deep blue for plunges far away from the XPT to yellow for plunges close to the XPT. The errorbars represent one standard deviation. The vertical black line and shaded gray region indicate the separatrix location and its uncertainty from magnetic reconstruction. The colored vertical dashed lines (shown in the first row only) indicate the location of the secondary separatrix of the SF discharges.

in the attached SF divertor may be related to the stronger flux expansion of the SF geometry, which could reduce parallel pressure gradients and spread the upstream pressure over a larger flux volume, leading to weaker flow acceleration and less peaked profiles near the separatrix.

The broadening of $v_\parallel$ at the onset of detachment complement the findings of this work: enhanced turbulent transport broadens the profiles upstream of the dissipative region, particles enter the divertor already radially dispersed, and convection then carries these broadened profiles through the divertor, causing the SOL plasma to move more uniformly as a bulk.

The parallel heat flux is next evaluated to quantify the relative roles of conduction and convection in carrying energy along the field lines. To estimate the conductive component $q_\parallel^{\mathrm{cond}}$, a constant parallel heat conductivity coefficient of $\kappa = 2000$ is used for the electrons while the ion channel is neglected since its corresponding coefficient, $\kappa = 60$, is more than an order of magnitude smaller and contributes negligibly to the total conductive flux [56]. The temperature gradient is computed directly from the measured T_{e} profiles along the field line. The convective component $q_\parallel^{\mathrm{conv}}$ is obtained using the measured n_{e} and $v_\parallel$ profiles, and the previously stated assumption of $T_{\mathrm{e}} = T_{\mathrm{i}}$.

Figure 11 shows the total (orange-red), conductive (blue), and convective (green) parallel heat fluxes for each divertor scenario. The solid lines represent the averaged profiles obtained from all probe plunges, while the shaded regions indicate the spread among different plunge data. Under attached conditions, the conductive term dominates the total parallel heat flux in the SOL, contributing between 74% and 93% of the total $q_\parallel$. In contrast, at the detachment onset, the conductive channel weakens as temperature gradients flatten, and the convective contribution exceeds 80% of the total $q_\parallel$. The reduction of $q_\parallel^{\mathrm{cond}}$ between the primary and secondary separatrixes of the SF at the detachment onset is greater than in the SN, illustrating the SF ability to further dissipate energy. These results confirm the transition inferred from the velocity measurements: in attached plasmas, the steep parallel temperature gradient sustains strong conductive transport, while in near-detached plasmas, the parallel motion of the bulk plasma becomes the principal carrier of energy toward the divertor target.

The transition from conduction- to convection-dominated transport as detachment develops is also seen in the poloidal projection of the parallel heat flux, $q_\parallel^\theta = q_\parallel \times B_\theta/B$. In the attached scenarios, $q_\parallel^\theta$ peaks in the near SOL between 400 and 600 kW m^{-2} in the SN, and around 400 kW m^{-2} in the SF, dominated by the electron conduction channel. In attached conditions, the poloidal $E \times B$ heat flux have been shown to reach up to ~ -280 kW m^{-2} in the SN and around half this value in the SF. While remaining smaller than the parallel conductive heat flux, $Q_\theta^{E\times B}$ represents a non-negligible fraction locally and highlights the role of cross-field convection in redistributing heat within the divertor leg. At the onset of detachment, the poloidal projection becomes convection dominated and nearly uniform, giving approximately 40 kW m^{-2} across the entire SOL and extending into the PFR in the SN,

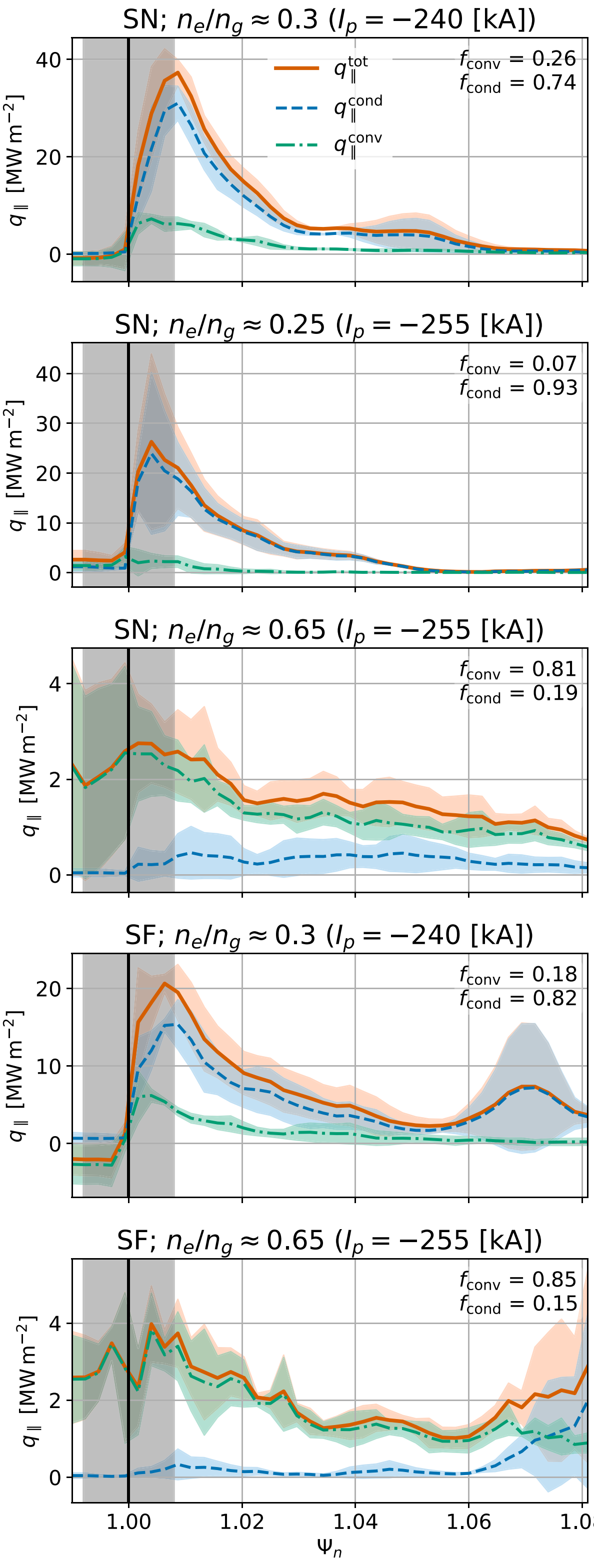

Figure 11. Total (orange-red), convective (green) and conductive (blue) heat fluxes carried by parallel transport in the divertor. Solid lines represent the mean fluxes, and the shaded regions indicate the spread arising from the different plunges. The fraction of convective (f_{conv}) and conductive (f_{cond}) contributions in the SOL are indicated for each divertor scenario.

and between 30 and 40 kW m^{-2} in the SF. The poloidal component of the parallel heat flux therefore dominates the total heat transport in the near SOL of the attached divertors while its contribution reduces at the onset of detachment.

8. Relative transport channel contributions to strike-point delivery

To quantify the relative strength of the studied transport channels in the outer divertor leg, we use the probe plunge closest to the divertor floor as a near-target reference plane in each plasma scenario. This choice is motivated by two observations: (i) the measured saturation current density profile $J_{\mathrm{SAT}}(\psi_n)$ at the probe is consistent with the floor-probes J_{SAT} within uncertainty, and (ii) $I_{\mathrm{SAT}}(\psi_n)$ (and therefore $J_{\mathrm{SAT}}(\psi_n)$) changes weakly as the probe approaches the divertor floor as seen in figure 4. Together, these indicate that the parallel particle throughput in the strike-point-connected SOL band is approximately conserved between the near-floor probe plane and the target. The near-floor probe measurements therefore provide a practical reference for strike-point delivery. In contrast, the electron temperature is lower at the floor in attached conditions, while remaining comparable at the detachment onset. The target-normal particle and heat reference fluxes, respectively $\Gamma_{\perp,\mathrm{target}}$ and $q_{\perp,\mathrm{target}}$, are obtained from the floor-probe measurements using the local grazing angle α at the target surface.

To reduce sensitivity to the separatrix position and to focus on the strike-point-connected bundle, we use a near-separatrix interval $\psi_n \in [\psi_1, \psi_2]$, with $\psi_1 = 1.000$ and $\psi_2 = 1.008$, covering the uncertainty in the separatrix location in the SOL. We then define representative band-averaged flux densities as:

$$\left\langle X^{\Gamma,\,q} \right\rangle_{\psi_1:\psi_2} \equiv \frac{1}{\psi_2 - \psi_1} \int_{\psi_1}^{\psi_2} X(\psi_n)\, \mathrm{d}\psi_n, \qquad (11)$$

where X is the particle (X^{Γ}) or heat (X^{q}) flux being considered. We then quantify each channel relative to the delivered reference flux densities using band-averaged ratios; for particles:

$$\mathcal{P}^{(\Gamma)}\,[\%] = 100\, \frac{\left| \left\langle X^{\Gamma} \right\rangle_{\psi_1:\psi_2} \right|}{\left\langle \Gamma_{\perp,\mathrm{target}} \right\rangle_{\psi_1:\psi_2}}, \qquad (12)$$

and analogously for heat:

$$\mathcal{P}^{(q)}\,[\%] = 100\, \frac{\left| \left\langle X^{q} \right\rangle_{\psi_1:\psi_2} \right|}{\left\langle q_{\perp,\mathrm{target}} \right\rangle_{\psi_1:\psi_2}}. \qquad (13)$$

Equations (12) and (13) provide a measure of the local strength of each transport channel relative to the delivered fluxes to the outer strike point.

A practical distinction is required between the radial $E \times B$ and turbulent radial channels in the present near-target delivery

Table 3. Channel contributions to the normal particle flux target delivery.

	Attached			Detachment onset	
	SN ($I_\mathrm{p} = -240\,\mathrm{kA}$)	SN ($I_\mathrm{p} = -255\,\mathrm{kA}$)	SF ($I_\mathrm{p} = -240\,\mathrm{kA}$)	SN ($I_\mathrm{p} = -255\,\mathrm{kA}$)	SF ($I_\mathrm{p} = -255\,\mathrm{kA}$)
$\langle\Gamma_{\perp,\mathrm{target}}\rangle$ $\left(\times 10^{22}\mathrm{m}^{-2}\,\mathrm{s}^{-1}\right)$	2.28	1.97	2.56	3.85	3.17
$\mathcal{P}^{\widetilde{\Gamma}_\mathrm{r}}$ (%)	1.1	1.3	2.8	0.8	1
$\mathcal{P}^{\Gamma_\mathrm{r}^{E\times B}}$ (%)	9.5	11.1	0.75	0.61	4.4
$\mathcal{P}^{\Gamma_\theta^{E\times B}}$ (%)	26.2	29.5	13.75	2.26	3.97

Table 4. Channel contributions to the normal heat flux target delivery.

Term	Attached			Detachment onset	
	SN ($I_\mathrm{p} = -240\,\mathrm{kA}$)	SN ($I_\mathrm{p} = -255\,\mathrm{kA}$)	SF ($I_\mathrm{p} = -240\,\mathrm{kA}$)	SN ($I_\mathrm{p} = -255\,\mathrm{kA}$)	SF ($I_\mathrm{p} = -255\,\mathrm{kA}$)
$\langle q_{\perp,\mathrm{target}}\rangle$ $\left(\mathrm{MW\,m}^{-2}\right)$	0.38	0.44	0.29	0.17	0.14
$\mathcal{P}^{\widetilde{Q}_\mathrm{r}^\mathrm{conv}}$ (%)	0.35	0.35	1.2	0.27	0.16
$\mathcal{P}^{Q_\mathrm{r}^{E\times B}}$ (%)	16.79	14.45	2.13	0.78	4.26
$\mathcal{P}^{Q_\theta^{E\times B}}$ (%)	27.75	33.34	17.71	2.66	3.06

framework. The radial $E\times B$ flux is inferred from an inter-plunge electric-field estimate as in section 6.1. It therefore represents a divertor-leg-averaged radial drift rather than a local quantity at the lowest plunge. Using this leg-averaged $\Gamma_\mathrm{r}^{E\times B}$ and $Q_\mathrm{r}^{E\times B}$ is nonetheless appropriate because it captures the typical cross-field exchange experienced by the strike-point-connected bundle along the outer leg, and is taken between the lowest two probe plunges when the data permits. By contrast, the turbulent radial flux is strongly localized near the XPT. The near-XPT plunge primarily diagnoses upstream turbulent spreading that broadens profiles before parallel transport carries them toward the target. This is distinct physics from the near-target redistribution considered here. Consequently, we use the turbulent flux measured at the lowest plunge and do not interpret the large upstream $\widetilde{\Gamma}_\mathrm{r}$ observed near the XPT as a direct contributor to target delivery. This separation explains the small values of $\mathcal{P}^{\widetilde{\Gamma}_\mathrm{r}}$ and $\mathcal{P}^{\widetilde{Q}_\mathrm{r}^\mathrm{conv}}$ obtained, which indicate that near the target the turbulent radial channel is weak compared to the delivered parallel throughput, consistent with the profiles of $\widetilde{\Gamma}_\mathrm{r}$ away from the XPT shown in figure 7.

The ratios from equations (12) and (13) are reported in tables 3 and 4 respectively. In all cases, parallel transport remains the dominant pathway for particle and power delivery to the outer strike point. In attached conditions, the poloidal $E\times B$ particle flux is a significant contributor to target delivery, reaching $\mathcal{P}^{\Gamma_\theta^{E\times B}}\sim 30\%$ in the SN and $\sim$14% in the SF. The radial $E\times B$ particle flux contribution is smaller, around 10% in the SN and much lower, around 1%, in the SF. The turbulent radial particle transport remains comparatively weak, with $\mathcal{P}^{\widetilde{\Gamma}_\mathrm{r}}\sim 1\%$–$3\%$.

For heat, the DC $E\times B$ contributions are substantial in attached conditions, with $Q_\theta^{E\times B}$ reaching $\mathcal{P}^{Q_\theta^{E\times B}}\simeq 28\%$–$33\%$ in the SN and $\sim$18% in the SF, and $Q_\mathrm{r}^{E\times B}$ reaching $\mathcal{P}^{Q_\mathrm{r}^{E\times B}}\simeq$ 15%–17% in the SN but only 2% in the SF. The limited number of probe plunges in the attached SF could influence the low radial DC $E\times B$ ratio obtained. The turbulent convective heat flux contribution remains negligible across all attached and onset of detachment scenarios. At the detachment onset, the drift-driven particle redistribution terms decrease markedly, with both $\mathcal{P}^{\Gamma_\theta^{E\times B}}$ and $\mathcal{P}^{\Gamma_\mathrm{r}^{E\times B}}$ under 5%, and seemingly higher in the SF. The DC $E\times B$ heat fractions likewise drop to a few percent, highlighting the increasingly dominant role parallel transport has in delivering both particles and power to the outer strike point near detachment.

9. Conclusions

The RMS levels of plasma fluctuations remain comparable between SN and SF divertors in both attached and near-detached conditions, increasing with distance from the floor. The broadening of the RMS levels at the onset of detachment in both SN and SF divertors hints at faster radial transport of turbulent structures.

An increase in radial turbulent transport by a factor of $2-4$ is detected near the XPT and upstream of the dissipative region at the detachment onset in both SN and SF divertors. This increase is similar across configurations, reaching $\widetilde{\Gamma}_\mathrm{r}\approx 4\times 10^{21}\ \mathrm{m}^{-2}\mathrm{s}^{-1}$, and does not extend into the dissipative divertor, where $\widetilde{\Gamma}_\mathrm{r}$ remains comparable to attached conditions at $\sim 1\times 10^{21}\ \mathrm{m}^{-2}\mathrm{s}^{-1}$. This enhancement is the only transport mechanism identified in this study that is consistent with the expected increase in radial transport during detachment. In combination with the increased λ_n in both SN and SF near-detached divertors in the vicinity of the XPT, these results suggest that particles enter the divertor region already radially spread by turbulent transport above the dissipative region. Convection then transport the plasma through the divertor uniformly across the SOL, as seen from the broadening of the $M_{\|}$ and $v_{\|}$ profiles.

The transition toward convective parallel flows is accompanied by a corresponding shift in the heat transport balance, with the convective contribution exceeding 80% of the total parallel heat flux at the detachment onset, while the conductive channel dominates under attached conditions. This shift underscores the central role of convective processes in carrying both particles and energy through the divertor when approaching detachment.

Normalizing the measured cross-field transport channels in the outer divertor leg to the target-normal fluxes showed that drift-driven convection is a significant transport channel in the target-proximate region under attached conditions, weakening at the detachment onset. In the attached divertors, the poloidal $E\times B$ particle flux reaches ∼14%–30% of $\Gamma_{\perp,\mathrm{target}}$ and the radial $E\times B$ particle flux reaches ∼1%–11%, while turbulent radial particle transport remains weak (∼1%–3%). For heat, $Q_{\theta}^{E\times B}$ and $Q_{\mathrm{r}}^{E\times B}$ reach respectively ∼30% and ∼15% of $q_{\perp,\mathrm{target}}$, whereas the turbulent convective heat flux remains negligible. At the detachment onset, these drift-driven contributions drop markedly for both particles and heat to only a few percent of the target delivery, indicating a transition toward increasingly parallel-dominated delivery to the outer strike point in the target-proximate region.

Finally, the evolution of the V_{f} and V_{p} profiles from attached to near-detached conditions highlights the role of plasma currents in setting the electric field structure. In the studied scenarios, rearrangement of the plasma currents at the detachment onset effectively reduced the DC drifts in the SOL and altered the E_{θ} structure in the PFR. These findings stress the importance of accounting for plasma currents when analyzing drift dynamics in divertor plasmas.

Acknowledgments

This work was supported by the U.S. Department of Energy under Grants No. DE-SC0010529 and No. DE-FG02-07ER54917. Work on this submission has received additional funding from Grant No. DE-NA0003525.

This work has been carried out within the framework of the EUROfusion Consortium, partially funded by the European Union via the Euratom Research and Training Programme (Grant Agreement No 101052200 — EUROfusion). The Swiss contribution to this work has been funded by the Swiss State Secretariat for Education, Research and Innovation (SERI). Views and opinions expressed are however those of the author(s) only and do not necessarily reflect those of the European Union, the European Commission or SERI. Neither the European Union nor the European Commission nor SERI can be held responsible for them.

ORCID iDs

Rabel Rizkallah 0000-0003-1794-2371
Jose A. Boedo 0000-0003-2230-4112
Cedric K. Tsui 0000-0002-7346-8312
Renato Perillo 0000-0001-6696-5970

References

[1] Loarte A. *et al* 2007 Chapter 4: Power and particle control *Nucl. Fusion* **47** S203
[2] Eich T. *et al* (ASDEX Upgrade Team and JET EFDA Contributors) 2013 Scaling of the tokamak near the scrape-off layer H-mode power width and implications for ITER *Nucl. Fusion* **53** 093031
[3] Zohm H. *et al* 2013 On the physics guidelines for a tokamak DEMO *Nucl. Fusion* **53** 073019
[4] Boedo J., McLean A.G., Rudakov D.L. and Watkins J.G. 2018 A review of direct experimental measurements of detachment *Plasma Phys. Control. Fusion* **60** 044008
[5] Leonard A.W. 2018 Plasma detachment in divertor tokamaks *Plasma Phys. Control. Fusion* **60** 044001
[6] Pitts R. *et al* 2019 Physics basis for the first ITER tungsten divertor *Nucl. Mater. Energy* **20** 100696
[7] Reimold F. *et al* 2015 Experimental studies and modeling of complete H-mode divertor detachment in ASDEX Upgrade *J. Nucl. Mater.* **463** 128–34
[8] Meier E., Covele B., Guo H., Leonard A. and Thomas D. 2020 Modeling $E\times B$ drift transport in conceptual slot divertor configurations *Contrib. Plasma Phys.* **60** e201900151
[9] Potzel S., Wischmeier M., Bernert M., Dux R., Müller H. and Scarabosio A. 2013 Characterization of the fluctuating detachment state in ASDEX Upgrade *J. Nucl. Mater.* **438** S285–90
[10] Fenstermacher M.E. *et al* 1997 Comprehensive 2D measurements of radiative divertor plasmas in DIII-D *J. Nucl. Mater.* **241-243** 666–71
[11] Terry J., Ballinger S., Brunner D., LaBombard B., White A. and Zweben S. 2017 Fast imaging of filaments in the X-point region of Alcator C-Mod *Nucl. Mater. Energy* **12** 989–93
[12] Scotti F., Zweben S., Soukhanovskii V., Baver D. and Myra J. 2018 Divertor leg filaments in NSTX-U *Nucl. Fusion* **58** 126028
[13] Wüthrich C. *et al* (the TCV Team) 2022 X-point and divertor filament dynamics from gas puff imaging on TCV *Nucl. Fusion* **62** 106022
[14] Wüthrich C. *et al* (the TCV Team) 2024 Dependence of divertor turbulence on plasma density and current in TCV *Nucl. Fusion* **65** 016011
[15] Krasheninnikov S.I. and Smolyakov A.I. 2016 Current convective instability in detached divertor plasma *Phys. Plasmas* **23** 092505
[16] Stepanenko A.A. and Krasheninnikov S.I. 2018 Numerical study of the current-convective instability driven by asymmetry of detachment in inner and outer divertors *Phys. Plasmas* **25** 012305
[17] Krasheninnikov S., Rensink M., Rognlien T., Kukushkin A., Goetz J., LaBombard B., Lipschultz B., Terry J. and Umansky M. 1999 Stability of the detachment front in a tokamak divertor *J. Nucl. Mater.* **266-269** 251–7
[18] Krasheninnikov S.I. and Kukushkin A.S. 2017 Physics of ultimate detachment of a tokamak divertor plasma *J. Plasma Phys.* **83** 155830501
[19] Yang H. *et al* (the TCV Team) 2023 Numerical study of divertor detachment in TCV H-mode scenarios *Plasma Phys. Control. Fusion* **65** 125005
[20] Krasheninnikov S.I., Sigmar D.J. and Yushmanov P.N. 1995 Effect of $E\times B$ drift on divertor plasma flows *Phys. Plasmas* **2** 1972–5
[21] Rognlien T., Porter G. and Ryutov D. 1999 Influence of $E\times B$ and ∇B drift terms in 2-D edge/SOL transport simulations *J. Nucl. Mater.* **266-269** 654–9
[22] Rognlien T.D., Ryutov D.D., Mattor N. and Porter G.D. 1999 Two-dimensional electric fields and drifts near the magnetic separatrix in divertor tokamaks *Phys. Plasmas* **6** 1851–7

[23] Moyer R., Lehmer R., Boedo J., Watkins J., Xu X., Myra J., Cohen R., D'Ippolito D., Petrie T. and Schaffer M. 1999 Potentials, $E \times B$ drifts and fluctuations in the DIII-D boundary *J. Nucl. Mater.* **266-269** 1145–50

[24] Boedo J.A., Schaffer M.J., Maingi R. and Lasnier C.J. 2000 Electric field-induced plasma convection in tokamak divertors *Phys. Plasmas* **7** 1075–8

[25] Schaffer M., Boedo J., Moyer R., Carlstrom T. and Watkins J. 2001 Large $E \times B$ convection near the divertor X-point *J. Nucl. Mater.* **290-293** 530–6

[26] Schaffer M.J. *et al* 2001 $E \times B$ circulation at the tokamak divertor X-point *Phys. Plasmas* **8** 2118–24

[27] Tsui C.K., Boedo J.A., Février O., Reimerdes H., Colandrea C. and Gorno S. (the TCV Team) 2022 Relevance of $E \times B$ drifts for particle and heat transport in divertors *Plasma Phys. Control. Fusion* **64** 065008

[28] De Oliveira H., Theiler C., Février O., Reimerdes H., Duval B., Tsui C., Gorno S., Oliveira D. and Perek A. (the TCV Team) 2022 New insights on divertor parallel flows, $E \times B$ drifts and fluctuations from in situ, two-dimensional probe measurement in the tokamak á configuration variable *Nucl. Fusion* **62** 096028

[29] Jaervinen A.E. *et al* 2018 $E \times B$ flux driven detachment bifurcation in the DIII-D tokamak *Phys. Rev. Lett.* **121** 075001

[30] Ryutov D.D. 2007 Geometrical properties of a 'snowflake' divertor *Phys. Plasmas* **14** 064502

[31] Ryutov D.D., Cohen R.H., Rognlien T.D. and Umansky M.V. 2008 The magnetic field structure of a snowflake divertor *Phys. Plasmas* **15** 092501

[32] Ryutov D.D. and Soukhanovskii V.A. 2015 The snowflake divertor *Phys. Plasmas* **22** 110901

[33] D'Ippolito D.A. and Myra J.R. 2006 Thermal transport catastrophe and the tokamak edge density limit *Phys. Plasmas* **13** 062503

[34] Myra J.R., Russell D.A. and D'Ippolito D.A. 2006 Collisionality and magnetic geometry effects on tokamak edge turbulent transport. I. A two-region model with application to blobs *Phys. Plasmas* **13** 112502

[35] Maurizio R., Tsui C., Duval B., Reimerdes H., Theiler C., Boedo J., Labit B., Sheikh U. and Spolaore M. (The TCV Team and The EUROfusion MST1 Team) 2018 The effect of the secondary X-point on the scrape-off layer transport in the TCV snowflake minus divertor *Nucl. Fusion* **59** 016014

[36] Giacomin M., Stenger L. and Ricci P. 2020 Turbulence and flows in the plasma boundary of snowflake magnetic configurations *Nucl. Fusion* **60** 024001

[37] Reimerdes H. *et al* (the TCV Team) 2013 Power distribution in the snowflake divertor in TCV *Plasma Phys. Control. Fusion* **55** 124027

[38] Walkden N.R., Labit B., Reimerdes H., Harrison J., Farley T., Innocente P. and Militello F. (the TCV Team and the MST1 Team) 2018 Fluctuation characteristics of the TCV snowflake divertor measured with high speed visible imaging *Plasma Phys. Control. Fusion* **60** 115008

[39] Tsui C.K., Boedo J.A., Myra J.R., Galassi D. and Wüthrich C. (the TCV Team) 2024 Divertor turbulent transport in the single null and snowflake in the TCV tokamak *Phys. Plasmas* **31** 022506

[40] Hofmann F. *et al* 1994 Creation and control of variably shaped plasmas in TCV *Plasma Phys. Control. Fusion* **36** B277

[41] Boedo J.A., Crocker N., Chousal L., Hernandez R., Chalfant J., Kugel H., Roney P. and Wertenbaker J. (the NSTX Team) 2009 Fast scanning probe for the NSTX spherical tokamak *Rev. Sci. Instrum.* **80** 123506

[42] Rudakov D.L. *et al* 2002 Fluctuation-driven transport in the DIII-D boundary *Plasma Phys. Control. Fusion* **44** 717

[43] Bickerton R. 1973 Particle diffusion due to fluctuations in toroidal systems *Nucl. Fusion* **13** 290

[44] Liewer P.C. 1985 Measurements of microturbulence in tokamaks and comparisons with theories of turbulence and anomalous transport *Nucl. Fusion* **25** 543

[45] Hutchinson I.H. 1988 Ion collection by probes in strong magnetic fields with plasma flow *Phys. Rev. A* **37** 4358–66

[46] Chung K.-S. and Hutchinson I.H. 1988 Kinetic theory of ion collection by probing objects in flowing strongly magnetized plasmas *Phys. Rev. A* **38** 4721–31

[47] Braginskii S.I. 1965 Transport processes in a plasma *Reviews of Plasma Physics* vol 1, ed M.A. Leontovich (Consultants Bureau) pp 205–311

[48] Moret J.-M., Duval B., Le H., Coda S., Felici F. and Reimerdes H. 2015 Tokamak equilibrium reconstruction code LIUQE and its real time implementation *Fusion Eng. Des.* **91** 1–15

[49] Tsui C.K. *et al* 2017 Poloidal asymmetry in the narrow heat flux feature in the TCV scrape-off layer *Phys. Plasmas* **24** 062508

[50] Loizu J., Morales J.A., Halpern F.D., Ricci P. and Paruta P. 2017 Scrape-off-layer current loops and floating potential in limited tokamak plasmas *J. Plasma Phys.* **83** 575830601

[51] Leonard A.W. *et al* 1997 Distributed divertor radiation through convection in DIII-D *Phys. Rev. Lett.* **78** 4769–72

[52] Leonard A.W. *et al* 1998 Radiative divertor plasmas with convection in DIII-D *Phys. Plasmas* **5** 1736–43

[53] Leonard A., Mahdavi M., Lasnier C., Petrie T. and Stangeby P. 2012 Scaling radiative divertor solutions to high power in DIII-D *Nucl. Fusion* **52** 063015

[54] LaBombard B., Conn R., Hirooka Y., Lehmer R., Leung W., Nygren R., Ra Y., Tynan G. and Chung K. 1989 Presheath profiles in simulated tokamak edge plasmas *J. Nucl. Mater.* **162-164** 314–21

[55] Boedo J.A., Porter G.D., Schaffer M.J., Lehmer R., Moyer R.A., Watkins J.G., Evans T.E., Lasnier C.J., Leonard A.W. and Allen S.L. 1998 Flow reversal, convection and modeling in the DIII-D divertor *Phys. Plasmas* **5** 4305–10

[56] Stangeby P.C. 2000 *The Plasma Boundary of Magnetic Fusion Devices* 1st edn (CRC Press) (https://doi.org/10.1201/9780367801489)